

Aperiodicity in the Near-field of Full-scale Rotor Blade Tip Vortices

Kolja Kindler · Karen Mulleners · Hugues Richard ·
Berend G. van der Wall · Markus Raffel

Received: date / Accepted: date

Abstract Blade tip vortices are the dominant vortical structures of the helicopter flow field. The inherent complexity of the vortex dynamics has led to an increasing interest in full-scale *in situ* experiments, where the near-field, closely behind the blade, is of particular interest, since measures of vortex control mostly target this initial stage of development. To examine the near-field, three-component Particle Image Velocimetry (PIV) measurements of blade tip vortices of a full-scale helicopter in simulated hover flight in ground effect were conducted. A feasible and robust evaluation procedure was developed to minimise the shortcomings of full-scale PIV applications, such as a moderate spatial resolution and an elevated measurement noise level. At vortex ages ranging from $\psi_v = 1^\circ$ to 30° , a pronounced aperiodicity and asymmetry of the vortex were observed in cross-sections perpendicular to the vortex axes. At $\psi_v = 1^\circ$ a preferential orientation of the vortex was observed. For increasing wake age, vortex wandering increased while the asymmetry of the vortex cores decreased. The high level of aperiodicity and core asymmetry must be taken into account when considering phase averaged vortex characteristics in the near wake region.

Keywords blade tip vortex · PIV · full-scale testing · aperiodicity

K. Kindler (✉) · K. Mulleners · H. Richard · M. Raffel
German Aerospace Centre (DLR), Bunsenstr. 10, 37073
Göttingen, Germany
B. G. van der Wall
German Aerospace Centre (DLR), Lilienthalplatz 7, 38108
Braunschweig, Germany
Present address: K. Kindler
Max Planck Institute for Marine Microbiology, Celsiusstr. 1, 28359
Bremen
E-mail: kkindler@mpi-bremen.de

PACS 47.80.Cb · 47.85.Gj

Symbols

a, b	principle axes [m]
A	amplitude
c	chord length [m]
\hat{e}_z	unit vector in z
C_T	thrust coefficient
L_m	measurement volume length [m]
M	reference point in S ; magnification
Ma	Mach number
N_x	number of x
pdf	probability distribution function
P	point
r_c	core radius [m]
R	rotor radius [m]
Re	Reynolds number [m]
S	two-dimensional area [m ²]
t	time [s]
T	thrust [N]
U	velocity [m s ⁻¹]
V_r, V_z, V_θ	radial, axial, tangential velocity [m s ⁻¹]
x, y, z	spatial coordinates [m]
α	flapping angle [°]
β	angle [°]
Γ_1	scalar function
Γ_v	circulation [m ² s ⁻¹]
δx	standard deviation of x
Δx	discrete step in x
ϵ	eccentricity
ϵ_c	eccentricity of the conditional average
θ	azimuth [°]
λ_2	flow field operator [rad s ⁻¹]
ν	viscosity [m ² s ⁻¹]
σ	solidity

ψ_v	rotor azimuth [$^\circ$]
ω	vorticity [s^{-1}]
Ω	angular velocity [rad s^{-1}]
$\bar{\cdot}$	conditional average operator

1 Introduction

The tip vortices trailing from helicopter rotor blades are the dominant and most conspicuous flow features of the rotor wake. Tip vortices are formed from intertwining shear layer vortices originating from the blade tip (Leishman 2001; Green and Acosta 1991). Due to their impact on acoustics, vibration levels, and rotorcraft performance, tip vortices have drawn considerable attention over the last decades (Landgrebe 1986; McCroskey 1995; Conlisk 2001).

The present knowledge of tip vortex dynamics is mainly based on extensive small-scale investigations (e.g. Leishman et al 1995; Leishman 2001; McAlister 2004). The prediction of full-scale vortex dynamics and interactions remains elusive because not all relevant dimensionless parameters can be attained in small-scale testing. For example, realistic vortex Reynolds numbers $Re = \Gamma_v/\nu$ (with the circulation Γ_v and the kinematic viscosity ν) are not obtained in wind tunnel tests (Sarpkaya 1998). Therefore, it is appealing to adapt and implement available experimental methods to probe the blade tip vortex characteristics *in situ*, i.e. in flight. Furthermore, full-scale, in-flight experiments provide access to a much larger range of flight parameters than typically attainable in wind tunnel testing. Since the vortex dynamics in the vicinity of the blade have a profound effect on blade aerodynamics, a direct approach of the vortex development in the near field is particularly desirable especially with regard to issues of vortex control (Green 1995; AGARD 1996).

Due to the inherent complexity of the rotor environment, most of the available literature on tip vortex formation focusses on fixed wings. The flow field around the wing tip contains multiple vortical structures whose size and influence depend on a wide range of parameters including load distribution, tip shape, etc. (Katz and Galdo 1989; Shekarriz et al 1993; Karakus et al 2008). These vortex filaments roll-up into a separate large scale tip vortex by virtue of their self-induced velocity. This roll-up process starts at the leading edge and is found to be exceedingly rapid. The vortex flow is observed to become self-similar and axially symmetrical within approximately one to two chord lengths downstream of the trailing edge (Ramaprian and Zheng 1997; Birch et al 2003). However, on rotary wings the spanwise load

distribution and the structure of the near wake is substantially different (Mahalingam et al 2000; Komerath et al 2004). The dynamics of blade tip vortices during formation and in the near field are not entirely understood and the extent of the near-field, commonly estimated as $\psi_v \geq 45^\circ$ to 90° (Johnson 1980), remains to be determined.

To provide insights into the dynamics of full-scale tip vortices in the near field, three-component velocity measurements of full-scale blade tip vortices by means of stereoscopic Particle Image Velocimetry (PIV) were conducted. In continuation of the feasibility study by Richard and Raffel (2002), an evaluation procedure was developed which provided sufficient measurement fidelity to analyse the tip vortex structure. We focused on aperiodicity and axial asymmetry of the vortex during formation at wake ages ranging from $\psi_v = 1^\circ$ to 30° . Aperiodicity refers to the variations of the size, shape and position of the vortex at a given wake age for consecutive passage of the blades. Aperiodicity of fully developed vortices is caused by a combination of free stream turbulence (Baker et al 1974), self-induced motion due the interaction of the individual vortex filaments (W.J. Devenport and Follin 1996), and various vortex perturbations and instabilities (Singh and Uberoi 1976; Sarpkaya 1996). It increases with wake age and is believed to be less pronounced immediately behind the trailing edge of the blade. We used a simplified elliptical representation of cross-sections of the vortex cores whose eccentricity provided a measure for the asymmetry of the vortex.

During formation, the tip vortex converges towards axial symmetry. The evolution of the eccentricity indicates the progress of roll-up process, i.e the formation stage. The presented evaluation procedure allows for a differentiation of asymmetry and aperiodicity and their impact on conditional averages. In the vicinity $\psi_v = 1^\circ$ large eccentricity and a preferential orientation of the vortices indicated ongoing shear layer roll-up. Thereafter, vortex wandering increased while the asymmetry of the vortex cores decreased. When considering phase averages to deduce effective vortex parameters in the near field (Kindler et al 2007; Valla et al 2009), both asymmetry and aperiodicity effects must be taken into account.

2 Experimental Methods

2.1 Measurement Configuration

The main rotor of the test helicopter had $N_b = 4$ hingeless blades of rectangular planform with a radius of $R = 4.91$ m, a chord length of $c = 0.27$ m, a solidity of

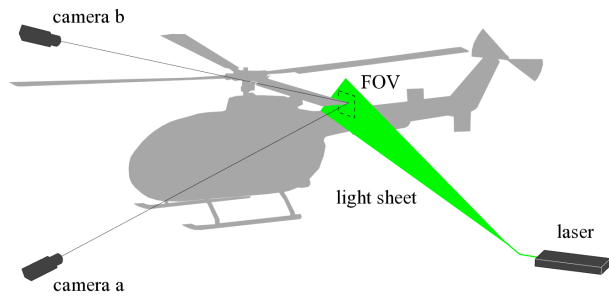


Fig. 1: Schematic representation of the experimental configuration for stereoscopic PIV measurements of the blade tip vortex on the test helicopter.

$\sigma = N_b c / (\pi R) = 0.07$, and -8° linear blade twist. The angular velocity of the main rotor was $\Omega = 44 \text{ rad s}^{-1}$ yielding a blade tip Mach number of $Ma = 0.64$. During simulated hover flight, the helicopter generated approximately $T \simeq 20000 \text{ N}$ thrust, corresponding to a thrust coefficient of $C_T = T / (\rho \pi \Omega^2 R^4) \simeq 0.0046$ resulting in a blade loading of $C_T / \sigma \simeq 0.066$.

The PIV measurement plane was located on the port-side, at 270° rotor azimuth (cf. figure 1). The data acquisition system consisted of two 10.7 Mpx CCD cameras equipped with 300 mm objectives in a stereoscopic configuration. The cameras were positioned on a vertical support; one 1.5 m above and the other 2.1 m below the rotor plane in idle condition at a distance of 10 m away from the observation area. Illumination of the flow field was provided by means of a laser light sheet fed by a double cavity Nd:Yag pulse laser with a wave length of 532 nm and an energy of 280 mJ per pulse. The laser sheet was vertically oriented in parallel to the trailing edge of the blade such that the tip vortices were measured in a plane approximately normal to their axes. The spatial resolution of the image acquisition system was 4 px mm^{-1} (corresponding to 1080 px c^{-1}) for a field of view (FOV) of $0.9 \text{ m} \times 0.6 \text{ m}$. The PIV system was synchronised with the main rotor taking advantage of an inductive rotor position indicator permanently installed for rotor balancing purposes.

When it comes to full-scale *in situ* PIV applications, the provision of a homogeneous and sufficiently dense tracer particle distribution is an extremely demanding task where the atmospheric background conditions play an important role. Even moderate cross-winds might strongly alter the optimal tracer injection point and the tracer density within the field of view. To compensate for effects of the ambient conditions, the tracer generation and supply system, including an injection nozzle reaching 3 m above the rotor disk, were installed on a mobile platform which could be relocated in response

to the outer conditions at a distance of one rotor radius away from the rotor disk. To obtain large tracer densities and a high injection volume flow, a purpose-built aerosol generator was deployed consisting of a total of fifty pressurised air supply lines, each of which was fitted with eight Laskin nozzles (1 mm in diameter), immersed in a 300 l volume of synthetic oil (Di-2-Ethyl-Hexyl-Sebacat, Merck). At a working overpressure of 0.1 MPa, highly concentrated, polydisperse droplets of approximately $1 \mu\text{m}$ in diameter were discharged at a flow rate of $400 \text{ m}^3 \text{ h}^{-1}$.

During the tests, ambient conditions were close to those of the International Standard Atmosphere (ISA) at an average temperature of 10°C and an atmospheric pressure of 1015 hPa, with calm winds below 1.5 m s^{-1} and intermittent gusts of less than 4 m s^{-1} .

2.2 Evaluation methodology

The evaluation methodology comprised three stages, velocity evaluation, vortex identification, and determination of the vortex shapes, each of which included a data validation procedure.

2.2.1 PIV evaluation

The stereoscopic PIV data were evaluated according to standard procedures (Raffel et al 2007). The acquired intensity images were high-pass filtered and normalised using the series minimum image prior to evaluation. A camera view misalignment correction was computed for each time series as part of the image de-warping, to compensate for small image offsets which otherwise would be greatly amplified due to the large-scale geometry of the set-up (Raffel et al 2004).

The interrogation window size and overlap were optimised according to the scheme of Richard et al (2006). The interrogation window size was minimised with respect to an acceptable signal-to-noise ratio while the sampling window overlap was maximised to avoid artificial smoothing of velocity gradients. The correlation analysis of the interrogation windows represents a low-pass filter limiting the peak velocities accessible (Richard et al 2006). By increasing the window overlap, the probability of an interrogation window being perfectly centred at the maximum velocity increases, minimising spatial averaging effects by the interrogation window itself. Additionally, a multi-grid evaluation scheme was used within the correlation analysis in order to further increase the spatial resolution in regions of strong shear. In this case, square cross-correlation windows of $32 \times 32 \text{ px}$ with an overlap of approximately 94% were used. The corresponding physical resolution,

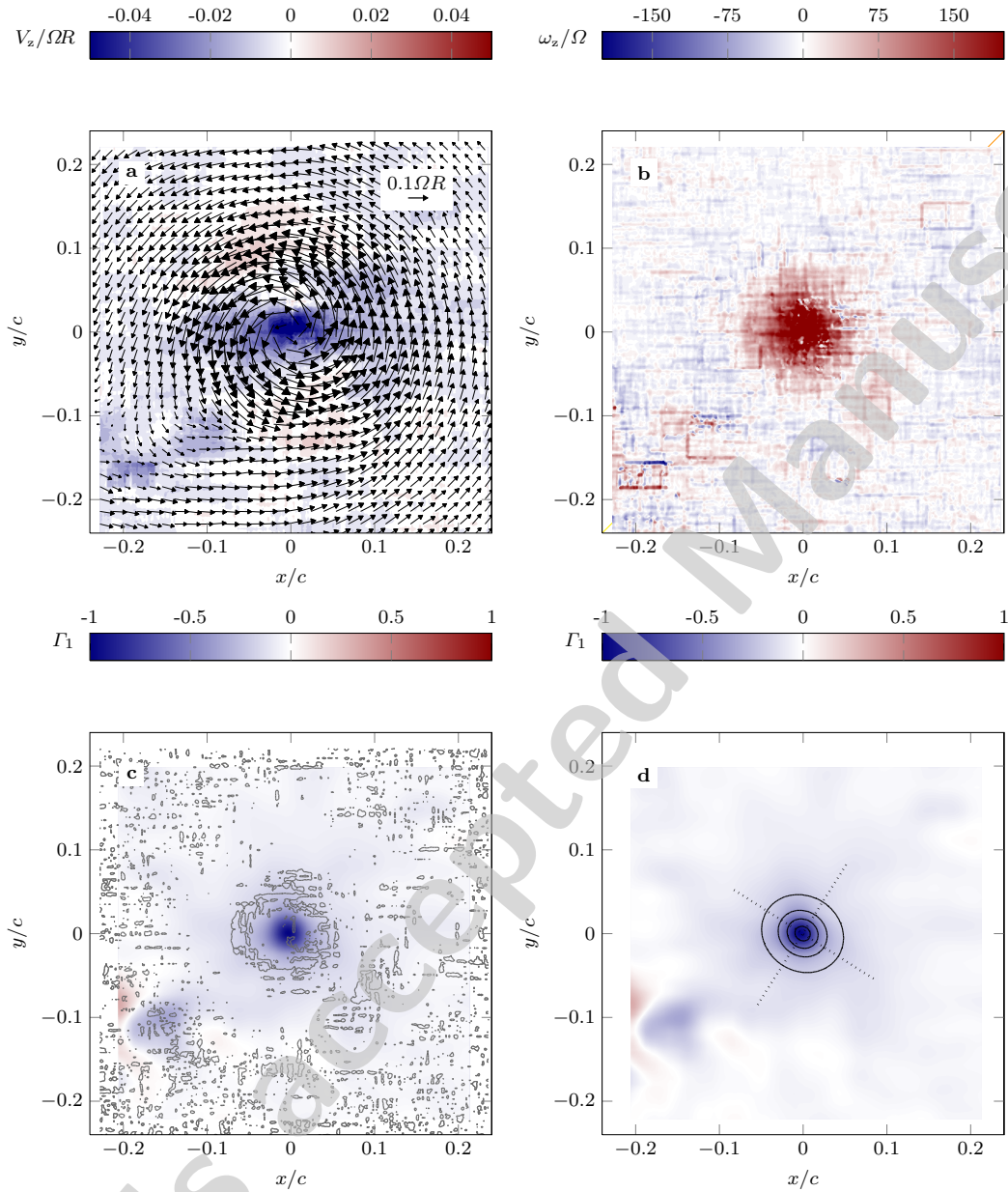


Fig. 2: A representative instantaneous velocity field (a) and the corresponding out-of-plane vorticity component (b) at $\psi_v = 5^\circ$. A combined representation of the scalar field Γ_1 (equation 1) and the contour lines of $\lambda_2 = 0$ for the same velocity field (c). The vortex core shape as derived by fitting equation 2 to Γ_1 where the dotted lines indicate the principle axes orientation (d).

i.e. the ratio of the PIV measurement volume to chord length, is $L_m/c = 0.0296$.

2.2.2 Vortex identification

Most common vortex identification schemes such as vorticity magnitude, λ_2 , etc., require the computation of velocity gradients which is undesirable for large-scale

PIV data. Elevated measurement noise can severely contaminate the velocity derivatives which is adverse to reliable vortex core identification by means of gradient-based criteria. For a comprehensive review of the robustness of various gradient and convolution based methods see van der Wall and Richard (2006) and Cucitore et al (1999).

In this work, the vortex centres were identified using the scalar function Γ_1 introduced by Graftieaux et al (2001) which is derived directly from the two-dimensional in-plane velocity field. In its discrete form it is defined as

$$\Gamma_1(P) = \frac{1}{N} \sum_S \frac{(PM \times U_M) \hat{e}_z}{\|PM\| \cdot \|U_M\|}, \quad (1)$$

where N is the number of points in the two-dimensional neighbourhood S of any given point P in the x, y plane, M lies in S , \hat{e}_z is the unit vector in z direction, and U_M is the in-plane velocity at M . The extremum of Γ_1 is identified with the location of the vortex axis (note that Γ_1 is not to be confused with the circulation). The averaged background velocities within the observation area were subtracted from the instantaneous fields prior to the analysis.

Vortex detection based on Γ_1 is much less susceptible to experimental noise which can be readily observed in figure 2. Γ_1 for the instantaneous velocity field was very clean (figure 2c), whereas the contour lines of $\lambda_2 = 0$ as well as the instantaneous out-of-plane vorticity component indicate a strong variability of the velocity gradients (figure 2b).

The absolute amplitude of the extremum of Γ_1 strongly depends on the integrity, i.e. coherence, of the vortical structure under consideration. Defining a lower limiting value $\Gamma_1 = 0.8$, incompletely captured vortices were discarded from the analysis.

2.2.3 Vortex asymmetry

The application of Γ_1 facilitated a robust and efficient assessment of the approximated vortex shapes. To analyse the vortex shape, the Γ_1 field was fitted with a bivariate Cauchy distribution of the form

$$L = \frac{A}{1 + \frac{(x - x_0)^2}{a} + \frac{(y - y_0)^2}{b}}, \quad (2)$$

where the coordinate pair (x_0, y_0) indicates the location of the vortex axis, A represents an arbitrary amplitude, and a and b are the principal axes of the approximated ellipse (cf. figure 2d). As an additional criterion to detect invalid vortex fields, the maximum allowed distance between the local extremum of Γ_1 and the centre of the bivariate Cauchy distribution was limited to two PIV sampling grid points in x and y direction, i.e. defining a maximum absolute deviation threshold of 1.4 mm.

To quantify the circularity of the vortex cores, we used the eccentricity

$$\epsilon = \sqrt{1 - (a/b)} \quad \text{with} \quad (a < b), \quad (3)$$

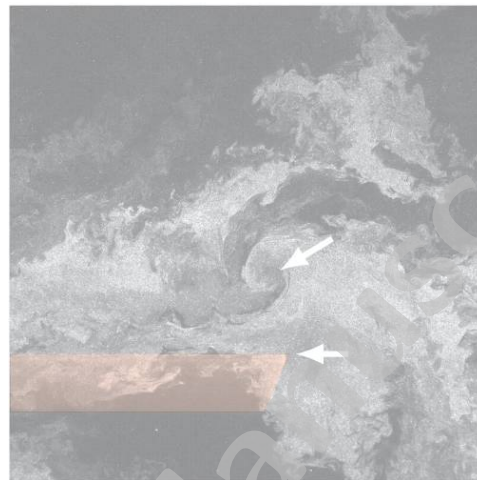


Fig. 3: An example of the tracer distribution within the region of interest at $\psi_v = 3^\circ$ as seen by the lower camera; the blade is highlighted and the blade tip and vortex centre are indicated by the arrows.

as a shape parameter. When ϵ is close to unity the vortex has a flat elliptical shape, approaching circularity when ϵ decreases towards zero.

2.3 Measurement accuracy

The quality of the full-scale PIV measurements was found to vary strongly for subsequent recordings. The overall measurement noise level was higher than typically obtained in laboratory experiments. These variations were primarily attributed to the varying or intermittently inhomogeneous tracer concentration including tracer density gradients within the region of interest (cf. figure 3). Due to the unsteady nature of the flow field, dissociated tracer patches of variable size were commonly found. Because the tracers are injected from above the rotor plane, the downwash tended to induce higher tracer concentrations inboard of the blade tip, while the fluid from the recirculation region outboards features stronger patchiness and, on average, lower tracer concentration.

The effect of tracer inhomogeneity on the data accuracy is threefold:

1. The velocity uncertainty of the PIV results was elevated. Using the standard deviation of particle dis-

ψ_v	1°	3°	5°	10°	20°	30°
N_{rf}	121	121	53	121	121	121
N_{vf}	45	108	45	105	69	78

Table 1: The number of acquired instantaneous N_{rf} and valid velocity fields N_{vf} for the range of wake ages measured.

placements within interrogation areas of size L_m^2 , the velocity uncertainty reads $\delta U = \delta X / (\Delta t M)$ (Raffel et al 2007), with the interframing time Δt and the image magnification M . For the present measurements $\delta U / (\Omega R) \leq 2\%$ for the in-plane velocity components was obtained. The noise level increased for the out-of-plane component to an uncertainty of 4%.

2. An areal lack of tracers resulted in non-physically dysmorphic or even undetectable vortex structures in the velocity fields. Vortex fields affected by areal defects were detected and discarded by successive application of the validation criteria described previously. The succession of validation steps after PIV evaluation, vortex detection, and shape approximation led to 11% to 63% of the time series data to be discarded (cf. table 1).
3. The local tracer density represented the intrinsic limit of measurement resolution as it defines the minimal interrogation window size, i.e. the spatial resolution or probe volume. In this case, $L_m/r_c = 0.593$, using $0.05c$ as an estimate of the vortex core radius, was close to the commonly accepted resolution requirement of $L_m/r_c < 0.5$ (Martin et al 2000).

3 Results and Discussion

Aperiodicity has many faces. One comprises the spatial fluctuations of the vortex axes location, i.e. vortex wandering. Another is concerned with the variation of the vortex core shapes. Both are addressed separately and their impact on phase averaged, i.e. effective, vortex parameters in the near field is assessed.

3.1 Vortex wandering

Vortex wandering is derived as the standard deviations of the spatial distribution of the vortex centre positions in x - and y -direction (figure 4). The blade tip position scatter is $\delta x/R = 1.1\%$, $\delta y/R = 3.0\%$. In the range $\psi_v = 1^\circ$ to 5° the scattering of the vortex positions largely conforms to the blade tip behaviour (figure 4). For larger ψ_v , vortex wandering increased continuously.

Vortex wandering in the near field is caused by external perturbation including background turbulence (Heyes et al 2003; Iungo et al 2009). With increasing wake age the vortex susceptibility to outer excitation increases. Additionally, small deviations in the near field are amplified which explains the observed growth.

The fluctuations of the tip vortex centre location were not isotropic but larger in normal than in spanwise direction. This anisotropy can be ascribed to the fact

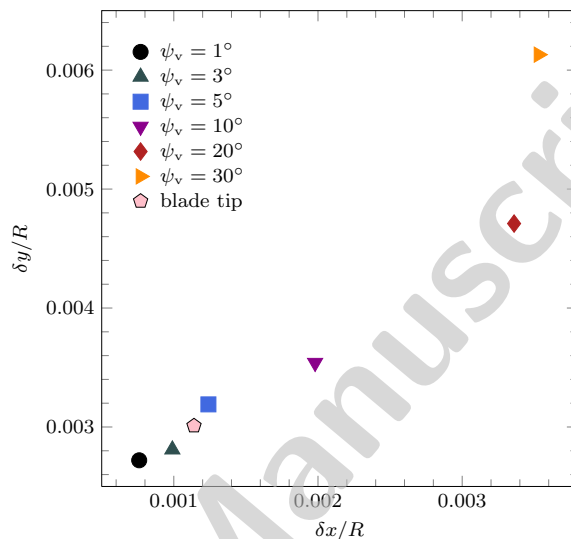


Fig. 4: The standard deviation of the vortex centre positions and the blade tip in the x, y plane.

that the flapping of the blade tip mainly imposed a vertical excitation.

3.2 Vortex asymmetry

In order to assess the vortex asymmetry, we consider the distribution of the eccentricity ϵ (equation 3) together with the major axes orientation, i.e. the inclination angle β with respect to the blade surface.

The distribution of eccentricity is approximately Gaussian, while β is uniformly distributed for $\psi_v \geq 3^\circ$ (figure 5). At $\psi_v = 1^\circ$ a preferential orientation was observed of approximately 35° directed upwards outboards which can be associated with the initial roll-up stage. At the same time, the eccentricity attained largest values. At the tip, the fluid on the suction side of the blade is pushed inboards while fluid from the pressure side moves outboards and winds upwards around the tip in response to the pressure difference. The flow is accelerated when moving from the pressure to the suction side causing the 35° orientation of the premature tip vortex.

For wake ages $\psi_v \geq 3^\circ$, no preferential orientation was found. With decreasing influence of the blade ($\psi_v \geq 3^\circ$), the velocity distribution outside the core region becomes increasingly uniform and the vortex tends towards a more circular shape (figure 6). The conditional average $\bar{\epsilon}$ of individual vortices remained on a high level over the entire range of wake ages attaining $\bar{\epsilon} \simeq 0.6$ for $\psi_v \geq 5^\circ$ corresponding to a principal axes ratio of ca. 0.64. This means that the vortices are non-circular with a large scatter in ϵ . Considering the con-

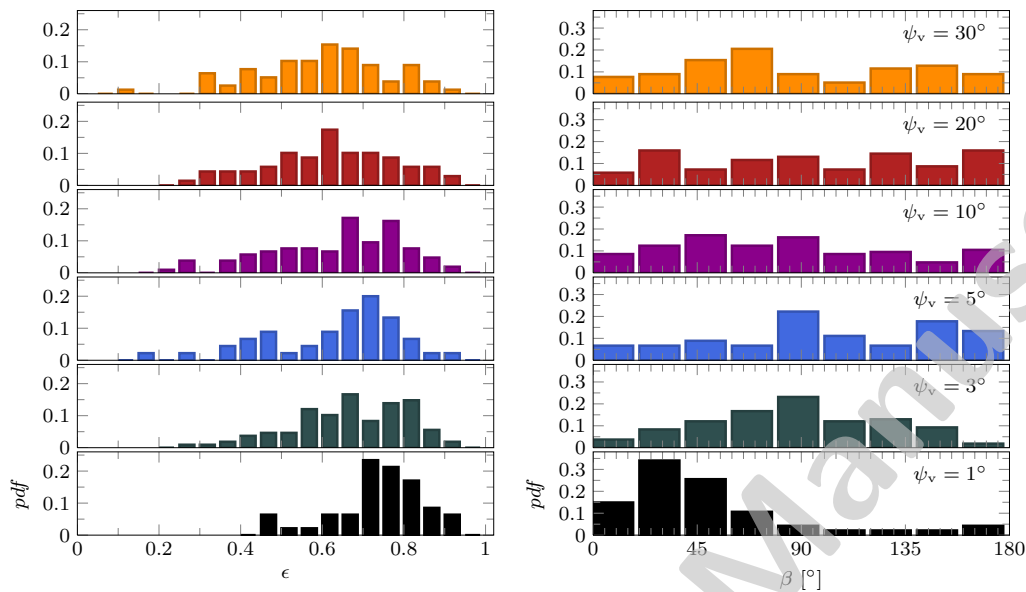


Fig. 5: Probability density function (*pdf*) of the vortex core eccentricity (left) and vortex core major axis orientation with respect to the horizontal (right).

ditionally averaged vortices, on the other hand, the eccentricity ϵ_c converges towards $\epsilon_c \approx 0.3$ at $\psi_v > 10^\circ$, corresponding to a principal axes ratio of ca. 0.91. Due to the arbitrary orientation of non-circular vortices, the conditionally averaged vortex field is smeared and increasingly circular. The notion of conditional average denotes the phase average including an alignment of individual vortex velocity fields with respect to their centre position.

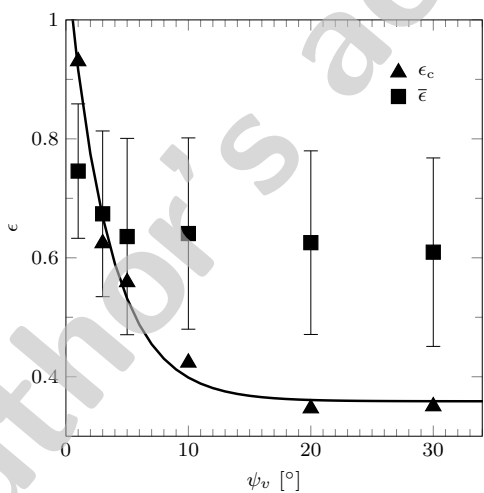


Fig. 6: The eccentricity ϵ_c of the conditionally averaged vortices together with the conditional averaged eccentricity $\bar{\epsilon}$ of the individual vortices; the solid line is a guide to the eye.

Our findings suggest ongoing shear-layer roll-up at $\psi_v = 1^\circ$ and convergence towards a well-defined vortex thereafter ($\psi_v \geq 3^\circ$). The fact that we do not observe a rapid convergence of the eccentricity towards 0 can be attributed to the following experimental constraints. First, the relatively small number of valid vortex fields considered might bias the statistics. Second, an inclination of the measurement plane with respect to the vortex axis might influence the derivation of vortex shapes. The inclination of the individual vortex axes with respect to the z -axis was estimated based on the out-of-plane plane velocity gradients ($\partial v/\partial x$, $\partial v/\partial z$) outside two times the core radius using an iterative procedure given by van der Wall and Richard (2006). The inclination angles were found to be smaller than 3.5° for the data relevant to this study which was considered negligible and a transformation into the vortex system was omitted.

3.2.1 Effective vortex parameters

In order to derive the effective vortex characteristics within the near field, conditionally averaged vortex velocity profiles were determined (figure 7). The conditional averaging comprised two steps. First, the instantaneous velocity fields ($v_\theta^n(r, \theta)$ and $v_z^n(r, \theta)$), were azimuthally averaged to obtain velocity profiles ($V_\theta^n(r)$ and $V_z^n(r)$) as a function of radial distance from the vortex centre. Second, the profiles at a given wake age were phase averaged to obtain the conditionally av-

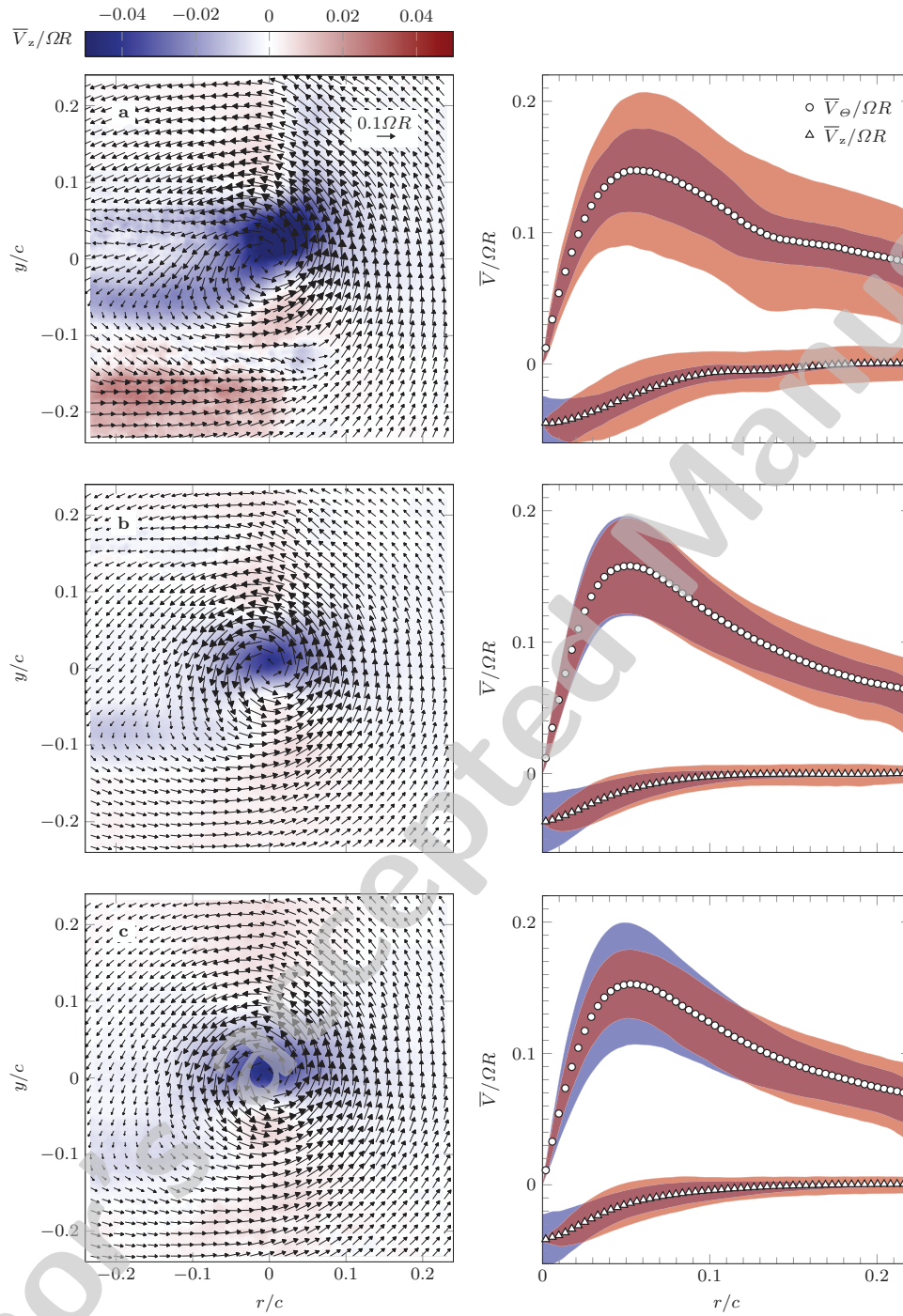


Fig. 7: Conditionally averaged vortex velocity fields (left) and the velocity profiles (right) at $\psi = 1^\circ$ (a), 3° (b), 5° (c), 10° (d), 20° (e), and 30° (f). The light red shading indicates deviations due to asymmetry ($\delta_1 V$ equation 4), the blue shading represents aperiodic deviations ($\delta_2 V$ equation 5), the superposition of both is dark red.

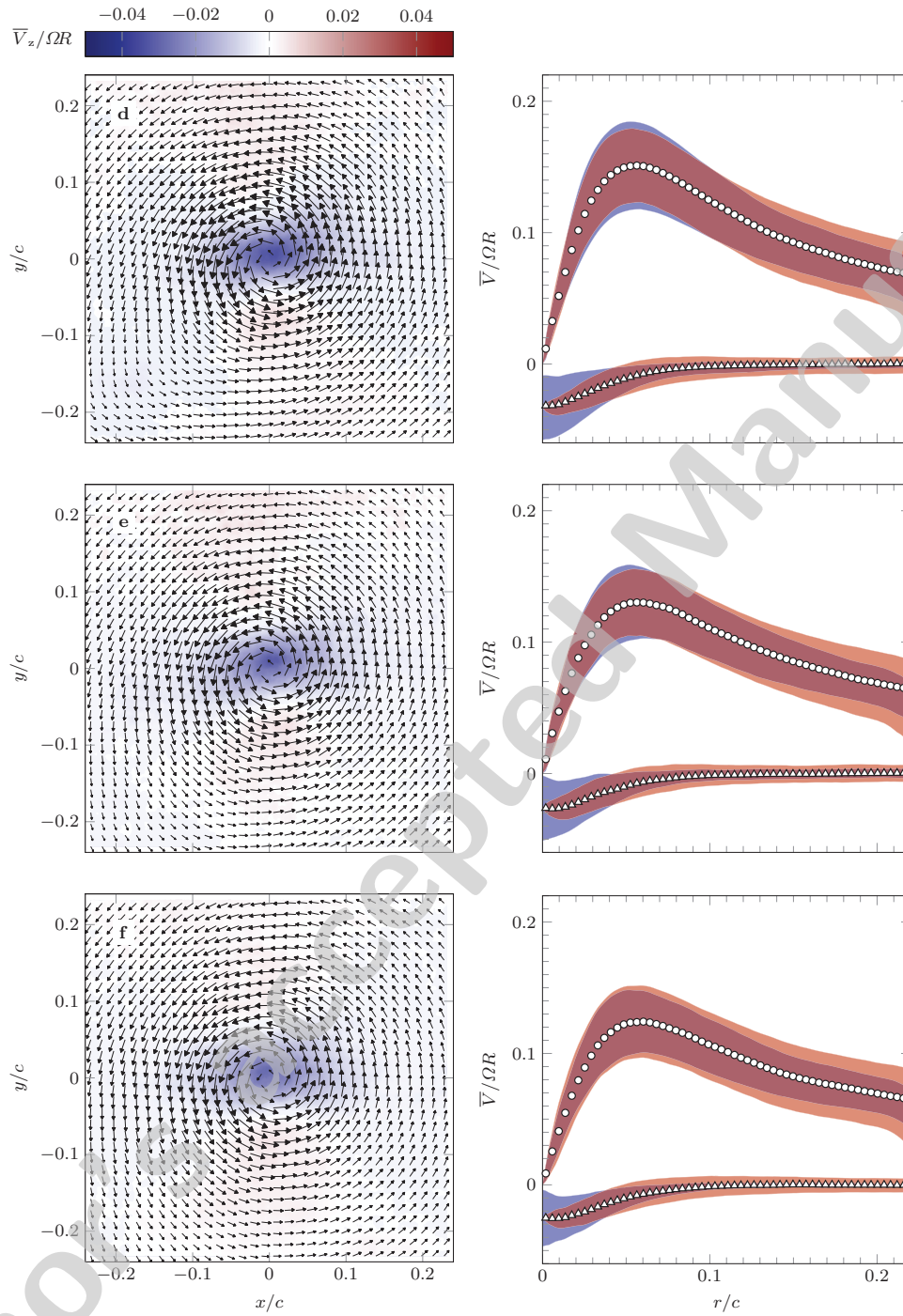


Fig. 7: Continued, for caption see facing page

eraged profiles $\bar{V}_\Theta(r)$ and $\bar{V}_z(r)$, respectively. With this procedure two different sources of uncertainty can be differentiated. The average asymmetry of individual vortices can be determined by averaging the standard deviation of azimuthal averages of individual vortex velocity fields

$$\delta_1 V(r) = \frac{1}{N_{\text{vf}}} \sum_{n=1}^{N_{\text{vf}}} \left[\frac{1}{N_\Theta} \sum_{i=1}^{N_\Theta} (v^n(r, \Theta_i) - V^n(r))^2 \right]^{\frac{1}{2}} \quad (4)$$

where Θ is the azimuthal angle with respect and N_Θ is the discretisation in azimuthal direction. Aperiodic variations within the time series, on the other hand, can be identified by the standard deviation of the azimuthally average of the conditionally averaged velocity field

$$\delta_2 V(r) = \left[\frac{1}{N_\Theta} \sum_{n=1}^{N_{\text{vf}}} (V^n(r) - \bar{V}(r))^2 \right]^{\frac{1}{2}} \quad (5)$$

where \bar{V} denotes conditional average.

For $\psi = 1^\circ$ the conditional average is mostly affected by the lack of axial symmetry while aperiodicity effects are small as expected for small wake ages ($\delta_1 V > \delta_2 V$, figure 7a). With increasing wake age, asymmetry decreases while aperiodicity increases (figure 7b – c). For $\psi_v = 10^\circ, 20^\circ$, and 30° both asymmetry and aperiodicity effects decrease (figure 7d – e). Within the near-field, for $\psi \geq 1^\circ$ the maximum swirl velocity $V_{\Theta, \text{max}}$ decreases, while the apparent core radius r_c (taken as the radius at which $V_\Theta(r_c) = V_{\Theta, \text{max}}$) increases. As the development progresses the vortex becomes more susceptible to external perturbations and instabilities, which could explain the increasing aperiodicity. As also seen in the eccentricity, a definite completion of the vortex formation stage cannot be inferred from the present data. However, only at $\psi_v = 1^\circ$ the roll-up is directly observed.

The effective vortex core radii for the range $\psi_v = 5^\circ$ to 30° increases from $r_c/c = 5.5\%$ to 6.6% while the maximum swirl velocity $V_\Theta/(\Omega R)$ decreases from 15% to 12% . The smearing of the conditional average leads to an overestimation of core radii of $\delta r_c/c \leq \epsilon^2$ of 36% while the peak swirl velocities $\delta V_\Theta/(\Omega R)$ are attenuated by averaging over a range of the same extent which yields an underestimation of 20% .

Another common feature of the conditionally averaged velocity fields was a noticeable, horizontal stretching of the cross-flow component (figure 7). This stretching was associated with the residual inclination of the vortex axes with respect to the measurement plane. It should also be noted that the extension of the cross-flow field to the lower left of figure 7a, b, and c represents

the drag bucket behind the rotor blade which is also visible in figure 2. Due to the blade circulation exhibiting a strong gradient towards the tip, a sheet of trailed vorticity is shed into the wake. Downstream from the trailing edge the blade wake continues to wind up into the vortex accompanied by a sheet of trailed vorticity distributed along the span of the blade.

The conditionally averaged vortex radius at $\psi_v = 3^\circ$ is found to be in agreement with corresponding results from Background Oriented Schlieren (BOS) measurements based on the same experimental configuration ($r_c/c = 5.5\%$ and 6% also at $\psi_v = 3^\circ$) (Kindler et al 2007). The conformity of the full-scale PIV and BOS results are attributed to the fact that the Schlieren measurements are equally effected by smearing due to aperiodicity. As a consequence, the asymmetry and aperiodicity must be taken into account in tip vortex investigations using integrative measurement techniques such as Schlieren methods or Light Detection and Ranging (Valla et al 2009).

4 Conclusions

Vortex velocity fields in the near-field of a full-scale helicopter rotor blade tip were presented and discussed, focusing on vortex core eccentricity within the formation stage and consequential aperiodicity effects. Only at $\psi_v = 1^\circ$ was a preferential vortex direction observed which can be associated with the initial roll up stage. At later wake ages vortex ellipticity of random orientation indicates ongoing vortex core relaxation. Thus, the initial stage of vortex roll-up appears to be completed closely behind the trailing edge of the blade, while the vortex equilibration persists over the entire range investigated (up to $\psi_v = 30^\circ$).

The application of large-scale PIV in conjunction with the evaluation methodology proposed here opens several possibilities in studying full-scale rotor tip vortex flows. Along with an investigation of fully developed tip vortex fields, future efforts will include time-resolved vortex trajectory measurements which are less susceptible to experimental noise.

Acknowledgements This work has been part of the European Commission funded project “Advanced In-Flight Measurement Techniques” (AIM) and the analysis has partly been performed in the framework of the US/German Memorandum of Understanding on Helicopter Aerodynamics, Task VIII “Rotor Wake Measurement Techniques”. The dedicated support by R. Gebhard and U. Göhmann from DLR’s flight facilities in Braunschweig as well as by our colleagues M. Jönsson and M. Kühn is gratefully acknowledged.

References

- AGARD (ed) (1996) The characterisation & modification of wakes from lifting vehicles in fluids, AGARD-CP-584
- Baker G, Barker S, Bofah K, Saffman P (1974) Laser anemometer measurements of trailing vortices in water. *J Fluid Mech* 65:325
- Birch D, Lee T, Mokhtarian F, Kafyke F (2003) Rollup and near-field behavior of a tip vortex. *J Aircraft* 40(3):6603
- Conlisk AT (2001) Modern helicopter rotor aerodynamics. *Prog in Aerospace Sci* 37:419
- Cucitore R, Quadrio M, Baron A (1999) On the effectiveness and limitations of local criteria for the identification of a vortex. *Eur J Mech B Fluids* 18(2):261–282
- Graftieaux L, Michard M, Grosjean N (2001) Combining PIV, POD and vortex identification algorithms for the study of unsteady turbulent swirling flows. *Meas Sci Technol* 12:1422
- Green S (ed) (1995) *Fluid Vortices*. Kluwer Academic Press
- Green S, Acosta A (1991) Unsteady flow in trailing vortices. *J Fluid Mech* 227:107
- Heyes A, Hubbard S, Marquis A, Smith D (2003) On the roll-up of a trailing vortex sheet in the very near field. *Proc IMechE Part G: J Aerospace Engineering* 217:263
- Iungo G, Skinner P, Buresti G (2009) Correction of wandering smoothing effects on static measurements of a winn-tip vortex. *Exp Fluids* 46:435
- Johnson W (1980) *Helicopter Theory*. Dover Publications, Mineoly, NY, USA
- Karakus C, Akilli H, Sahin B (2008) Formation, structure, and development of near-field wing tip vortices. *Proc IMechE Part G: J Aerospace Engineering* 222:13
- Katz J, Galdo JB (1989) Effect of roughness on rollup of tip vortices on a rectangular hydrofoil. *AIAA J* 26(3):247
- Kindler K, Goldhahn E, Leopold F, Raffel M (2007) Recent developments in background oriented Schlieren methods for rotor blade tip vortex measurements. *Exp Fluids* 43:233
- Komerath N, Wong O, Ganesh B (2004) On the formation and decay of rotor blade tip vortices. In: *Fluid Mechanics Meeting*, Portland, OR, June 2004
- Landgrebe A (1986) Overview of helicopter wake and airloads technology. In: *12th European Rotorcraft Forum*
- Leishman JG (2001) *Principles of helicopter aerodynamics*. Cambridge University Press, Cambridge, UK
- Leishman JG, Baker AM, Coyne AJ (1995) Measurement of rotor tip vortices using three-component LDV. *J Am Heli Soc* 41(4):342
- Mahalingam R, Wong O, Komerath N (2000) Experiments on the origin of tip vortices. In: *38th Aerospace Sciences Meeting and Exhibit*, Reno, NV, Jan. 10–13, 2000
- Martin PB, Pugliese JG, Leishman JG, Anderson SL (2000) Stereo PIV measurements in the wake of a hovering rotor. In: *American Helicopter Society 56th Annual Forum*, Virginia Beach, USA, May 2–4
- McAlister KW (2004) Rotor wake development during the first revolution. *J Am Heli Soc* 49:4
- McCroskey WJ (1995) Vortex wake of rotorcraft. In: *33th AIAA Aerospace Science Meeting and Exhibition*, Reno, USA, Jan. 9–12
- Raffel M, Seelhorst U, Willert C (2004) Recording and evaluation methods of PIV investigations on a helicopter rotor model. *Exp Fluids* 36:146
- Raffel M, Willert C, Wereley S, Kompenhans J (2007) *Particle image velocimetry, a practical guide*. Springer
- Ramaprian B, Zheng Y (1997) Measurements in rollup region of the tip vortex from a rectangular wing. *AIAA J* 45(12):1837
- Richard H, Raffel M (2002) Rotor wake measurements: full-scale and model tests. In: *American Helicopter Society 58th Annual Forum*, Montréal, Canada, June 11–13
- Richard H, Bosbach J, Henning A, Raffel M, van der Wall BG (2006) 2C and 3C PIV measurements on a rotor in hover condition. In: *13th International Symposium on Applications of Laser Techniques to Fluid Mechanics*, Lisbon, Portugal, June 26–29
- Sarpkaya T (1996) Vorticity, free surface, and surfactants. *Ann Rev Fluid Mech* 28:83
- Sarpkaya T (1998) Decay of wake vortices of large aircraft. *AIAA J* 36(9):1671
- Shekarriz A, Fu T, Katz J, Huang T (1993) Near-field behavior of a tip vortex. *AIAA J* 31(1):112
- Singh P, Uberoi M (1976) Experiments on vortex stability. *Phys Fluids* 19(12):1858
- Valla M, Augere B, Dolfi A, Goulard D, Fleury D (2009) 1.5 mm LIDAR for helicopter blade tip vortex measurements. In: *35th European Rotorcraft Forum*, Hamburg, Germany, Sep. 22–25
- van der Wall BG, Richard H (2006) Analysis methodology for 3C-PIV data of rotary wing vortices. *Exp Fluids* 40:798
- WJ Devenport SL, MC Rife, Föllin G (1996) The structure and development of a wing-tip vortex. *J Fluid Mech* 312:67–106